Topologically Allowed Nonsixfold Vortices in a Sixfold Multiferroic Material: Observation and Classification

Shaobo Cheng, Jun Li, Myung-Geun Han, Shiqing Deng, Guotai Tan, Xixiang Zhang, Jing Zhu, and Yimei Zhu

Topologically Allowed Non-Six-Fold Vortices in a Six-Fold Multiferroic Material: Observation and Classification

Shaobo Cheng[1,2], Jun Li[3], Myung-Geun Han[2], Shiqing Deng[1], Guotai Tan[4], Xixiang Zhang[3], Jing Zhu[1,*], and Yimei Zhu[2,*]

1. *School of Materials Science and Engineering, Tsinghua University, Beijing 100084, P. R. China*
2. *Department of Condensed Matter Physics and Materials Science, Brookhaven National Laboratory, Upton, NY 11973, USA*
3. *Division of Physical Science and Engineering, King Abdullah University of Science and Technology, Thuwal 239955, Kingdom of Saudi Arabia*
4. *Department of Physics, Beijing Normal University, Beijing 100875, P. R. China*

*: zhu@bnl.gov; jzhu@mail.tsinghua.edu.cn

Abstract

We report structural transformation of six-fold vortex domains into two-, four- and eight-fold vortices via a different type of topological defect in hexagonal manganites. Combining high-resolution electron microscopy and Landau-theory based numerical simulations, we investigate the remarkable atomic arrangement and the intertwined relationship between the vortex structures and the topological defects. The roles of their displacement field, formation temperature and nucleation sites are revealed. All conceivable vortices in the system are topologically classified using homotopy group theory and their origins are identified.

Topological structures, emerging near spontaneous symmetry-breaking transitions, are ubiquitously observed in wide branches of science.[1-6] In condensed matter, topologically protected defects can be promising candidates for information storage technology. Skyrmions, multiferroic vortices, domain walls, dislocations, and disclinations are examples, where emergent properties and behaviors have been reported.[7-12] Investigation of these stable configurations is of great interest due to their fascinating underlying physics responsible for striking geometric patterns found in order parameter (OP) field.[13] Understanding topological structures is crucial to the prediction of behavior and functionalities emerging from these topological defects.[14,15] However, to date, the interactions among topological defects have rarely been studied, largely due to the difficulties in experimental observation and validation. Understanding the interactions between topological defects might provide a new route to achieve programmable manipulation and control to yield emergent functionality.

In multiferroic hexagonal manganites $R\text{MnO}_3$ (R = rare-earth), the crystal structure adopts centrosymmetric $P6_3/mmc$ (D_{6h}) at high temperature. A structural transition occurs at temperature T_s, which lowers the symmetry to $P6_3cm$ (C_{6v}) mainly by the condensation of the K_3 phonon mode. This process leads to the trimerized tilting of MnO_5 bipyramids and corrugation of intercalated R layers while maintaining the six-fold symmetry (Fig. 1(a)). The condensation yields six possible azimuthal angles (φ) of the bipyramid tilting at an interval of $\pi/3$. Each value of φ is accompanied by a distinct corrugated configuration in R layers, in which two thirds of R atoms shift up along the c axis and the rest shift down, as summarized in Fig. 1(b).[16-18] Previous theoretical work suggests that the continuous symmetry of OP space at high-temperature gives rise to the formation of vortex cores, while the discrete Z_6 symmetry at low temperature leads to the emergence of six bounded domain walls surrounding each vortex core.[19-22] With continuous symmetry of the degeneracy OP space, φ varies continuously around the cores. At low temperature, φ falls into one of the six preferred values with equal probability, and Z_6 symmetry becomes dominant in the system.[19] This process results in the emergence of six crystallographically preferred domains denoted as α^+, β^-, γ^+, α^-, β^+, γ^- or α^+, γ^-, β^+, α^-, γ^+, β^- (known as vortex and anti-vortex) in sequence around the core.[16] These six-fold vortices are topologically protected and extremely stable under thermal perturbation and external biasing.[22-24] The distributions and connections of (anti)vortex cores have been analyzed by graph theory.[25,26] However, with the help of dislocations, the domain sequences around the vortex cores can be changed. Here, we report the first experimental observations of non-six-fold vortex cores in $R\text{MnO}_3$ using advanced electron microscopy to reveal their formation origin at atomic-scale.

The coupling mechanisms are studied by numerical simulations based on Landau theory, and vortices are topologically classified via homotopy group theory.

YMnO$_3$ single crystals were grown by floating zone method. Electron microscopy work was carried out at Brookhaven National Lab using the JEOL ARM 200CF microscope equipped with two aberration correctors achieving a point resolution of 0.08 nm. For HAADF (high-angle annular-dark-field) imaging, a convergent angle of 21.2 mrad and a collection angle of 67-275 mrad were used. To reduce noise, Wiener filter was used for some HAADF images.

Figure 1(c) illustrates a mesoscale composite of dark-field images of hexagonal YMnO$_3$, showing the coexistence of various 2-, 4-, 6- and 8-fold vortices (marked by red circles). The first-ever-observed eight-fold (anti)vortex is highlighted with the red rectangle. Figure 1(d) is the schematic of domain configurations derived from Fig. 1(c). Careful examination indicates the existence of partial edge dislocations (PEDs) near the vortex cores. In the floating zone method, a dramatic change in sample temperature during crystal growth might introduce PEDs.

Atomically resolved eight-fold and four-fold vortex structures are shown in Figs. 2(a) and (b).[27] In Fig. 2(a), domains with the same polarization direction and corrugation state are present in one vortex configuration (two α^-, β^- and $\gamma+$ domains in this case; energetically unstable in traditional six-fold vortices), can be stabilized by PEDs. Similar labeling was applied to other types of non-six fold vortices, including the four-fold vortex shown in Fig. 2(b). More analyses about the configurations of domain boundaries are also provided.[27] To map the associated strain field of the PEDs of the eight- and four-fold vortex cores, we used geometric phase analyses (GPA),[35] and the strain field of ε_{xx} (the x axis is [120] direction) around the PEDs in Figs. 2(a) and (b) were constructed from the atomic images. Clearly, the non-uniform displacement field near the vortex centers plays a significant role in altering the corrugated configuration of the vortex structure. The corresponding mesoscale dark-field images that possess dissimilar contrast for oppositely polarized ferroelectric domains due to the breaking of Friedel's law, are also included.[36] Careful atomic image analysis suggests that the PED possesses a Burgers vector of 1/3[120]. To avoid the energetically unfavorable configurations due to the presence of PEDs, the original 6-fold winding sequence $\alpha^- \rightarrow \beta^+ \rightarrow \gamma^- \rightarrow \alpha^+ \rightarrow \beta^- \rightarrow \gamma^+$ is transformed into a 4-fold winding $\alpha^- \rightarrow \beta^+ \rightarrow \gamma^- \rightarrow \beta^- \rightarrow \gamma^+$, and a four-fold domain is formed (Fig. 2(b)). All our experimentally observed non-six-fold vortices are summarized in Figs. 2(c)-(g), along with other three predicted configurations (Figs. 2(h)-(j)).

In RMnO$_3$, the formation process of six-fold vortices can be characterized by the variation of a two-component order-parameter field: tilting amplitude of MnO$_5$ bipyramids Q, and azimuthal angle φ.[19,22,37,38] The degeneracy OP space is composed of six distinct points at low temperature (Fig. 3(a)), and expands to the

continuous circle at a temperature slightly below T_s. The radius of this circle is proportional to the value of Q, so the circle shrinks into a single point when $T \geqslant T_s$ ($Q = 0$).[22] However, because of the additional structural displacement field induced by PEDs, these two components are not sufficient for depicting the domain patterns. We thus introduce another scalar order parameter θ for describing the *x*-component of the displacement field.[27] This parameter reflects the geometric phase around dislocations and is directly related to the atomic displacements of R atoms.[39-41] The distribution of θ around an edge dislocation with $b = 1$ and $\upsilon = 0.3$ is shown in Fig. 3(b): θ increases continuously from 0 to 2π along any clockwise circular-trajectory whose starting and ending point are on a dividing line (indicated in Fig. 3(b)) which is attached to the dislocation core. Considering this dislocation appears in a mono-domain ($\varphi = 0$), the "up-down-down" corrugated configuration above the dividing line abruptly switches into "down-down-up" below the line. The mismatch of corrugated configurations across the dividing line indicates that this line acts like an anti-phase domain wall which is not interlocked with ferroelectric boundaries. Since the dislocation is not perfect (for perfect case, $b = 3n$, n is an arbitrary integer), it is always bounded by such a line.[42,43] Thus, the corrugated configurations can be modulated by θ, and the OP space for RMnO$_3$ in which dislocations exist can be described by the surface of the cylinder (Fig. 3(c)). By topological transformation of this cylinder, a torus-like OP space V can be obtained (Fig. 3(d)). Hence, any closed loop in the system characterized by (Q, φ, θ) field can be precisely mapped into a continuous trajectory in V. More atomic models for 2-, 4-8-fold vortex core arrangements are provided.[27] Both experimental results and atomic models show that the corrugated configurations do not change significantly across dividing lines, because the lattice jump induced by dislocations is compensated by the changes of corrugated configuration at domain walls.

According to the homotopy group theory, for such a torus-like degeneracy space, all vortex configurations shown in Figs. 2(c)-(g) can be classified by elements (m, n) of the fundamental homotopy group $\pi_1(R) = Z \times Z$. [4,44,45] This homotopy group is different from the one presented in Ref. 19, which due to the expansion of OP space from one-dimensional circle to torus, under the effect of PEDs. Considering a clockwise loop surrounding the vortex core and its image trajectory in the OP space, the absolute value of integer m or n is the net number of times that the smaller or larger hole in the torus is circumnavigated by the trajectory, respectively. Values of m and n are positive when the circumnavigation directions are along the arrows indicated in Fig. 3(d), and negative when opposite the arrows. Based on this definition, n equals the Burgers vector b of the dislocation appearing in the core (for convenience, we treat two adjacent PEDs with $b = 1$ as one PED with $b = 2$). All vortex configurations shown in Fig. 2 can be classified accordingly (see caption of Fig. 2).

Generally, defects with lower winding numbers (i.e. smaller $|m|$ and $|n|$) are energetically preferred. It is also interesting to note that the number of ferroelectric domain walls bounded with a vortex core equals to $|6 \cdot m - 2 \cdot n|$.[27] Thus, a vortex core in our system should always be surrounded by an even number of domain walls.

To clarify the vortex-forming mechanism, we use the Landau phenomenological model for numerical simulations.[27] The newly defined angle parameter $(\varphi + \theta/3)$ ensures that the gradient energy density is continuous within domains, and dramatic variations take place only at ferroelectric domain walls and vortex cores. Based on this model, the annealing process can be simulated by Monte Carlo method.[22] Vortex configurations of Figs. 2(c)-(j) after annealing are shown in Figs. 4(a)-(h). The temperature at which dislocations form T_d plays an important role in determining different classes of vortices in these simulations.

When dislocations form above structural phase transition point T_s, classes of vortices labeled by $0 \times (\pm 1)$ and $0 \times (\pm 2)$ are those most frequently observed (Figs. 4(a) and 4(e)), and $(\pm 1) \times (\pm 1)$, $(\pm 1) \times (\mp 1)$, $(\pm 1) \times (\pm 2)$, and $(\pm 1) \times (\mp 2)$ types can be occasionally observed (Figs. 4(b)-(d) and 4(g)). In this case, the initial distribution of φ is arbitrary and θ is given. As temperature decreases from above T_s, the field of φ evolves adequately for lowering the local free energy. Thus the vortices with lowest energy can be obtained during this process. This suggests that the two-fold vortex with one dislocation in the core and four-fold vortex with two dislocations in the core are the most energetically preferred. As discussed in Ref. 22, the formation of six-fold vortex cores and domain walls in RMnO$_3$ takes place right at the structural phase transition temperature. So it is possible that the nucleation site of a vortex (i.e. the position around which φ varies from 0 to 2π continuously) is within or near a dislocation core region. In such a situation, vortices classified by $(\pm 1) \times n$ can be formed. Because of a higher gradient of the free energy density induced by a dramatically varying $(\varphi + \theta/3)$ field in the cores, compared with the vortices with $m = 0$, the value of Q decreases noticeably in these regions.

By lowering T_d $(T_d < \frac{2}{3} T_s)$, $(\pm 1) \times n$ type vortices become common and the eight-fold vortices classified by $(\pm 2) \times (\pm 2)$ can also be formed (Fig. 4(f)). At $T = T_d$, the six-fold vortex pattern has already been formed and the mobility of vortex cores and domain walls is much lower than that at high temperatures. To balance the increased free energy induced by the displacement field, only relatively high-energy vortices form, because the temperature is not sufficiently high to overcome the energy barrier blocking the formation of the $0 \times n$ type vortices. So, when one dislocation with $|b| = 2$ happens to locate within a six-fold vortex core at T_d, a $(\pm 2) \times (\pm 2)$ type

vortex forms. In addition, a new type of four-fold vortex classified by $(\pm 1) \times (\pm 2)$ is also frequently observed when $T_\mathrm{d} < \frac{2}{3} T_\mathrm{s}$. Though it belongs to the same class as the two-fold vortex shown in Fig. 4(d), the number of domain walls attached to the vortex core does not equal $|6 \cdot m - 2 \cdot n|$. This is because φ does not vary monotonically around the vortex core, and two separated areas have the same value of φ. However, these two areas can coalesce if they are near each other, and only two domain walls are left after merge. Thus, these two kinds of $(\pm 1) \times (\pm 2)$ vortices are topologically identical.

It is noteworthy that the core of $(\pm 2) \times (\pm 2)$ type vortex is not stable and tends to split into two adjacent vortices. For example, a 2×2 type vortex core can split into a 1×2 (both four-fold and two-fold vortices are possible) vortex core and a 1×0 (six-fold) vortex core. Increased T_d usually leads to greater distance between these cores. By comparing Figs. 4(i) and (j), it is obvious that the free energy density of the un-split eight-fold vortex core obtained at $T_\mathrm{d} = \frac{1}{6} T_\mathrm{s}$ is higher than the energies of those two split cores obtained at $T_\mathrm{d} = \frac{1}{2} T_\mathrm{s}$. This result explains the larger distance between two PEDs in eight-fold domain TEM image and why the $(\pm 2) \times (\pm 2)$ type eight-fold vortex is rarely seen in experiments.

In conclusion, using aberration-corrected electron microscopy we revealed startling detailed atomic configurations of crystallographically forbidden non-six-fold ferroelectric domains surrounding the vortex cores in hexagonal YMnO$_3$. The unanticipated symmetry breaking was found at both mesoscale (domains) and atomic scale (vortex cores) due to the intertwining of two types of topological defects, *i.e.* (anti)vortex cores and partial-edge-dislocations (PEDs). We show that due to the interaction of PEDs with surrounding lattice, the initially topologically protected 6-fold (anti)vortex core structures can be transformed into other configurations. Thus, PED, depending on its characteristics, including Burgers vector, formation temperature and nucleation sites, can behave as a control knob for regulating vortex domain symmetry. The ability to manipulate and control the ferroic orders in RMnO$_3$ in correlation with spontaneous magnetization, electric polarization, and spontaneous strain may provide a platform for exploring emerging physical phenomena with novel applications via topological defects.

Acknowledgement

China Scholarship Council. The samples were prepared through use of the resources of National Center for Electron Microscopy in Beijing. The theoretic work was done at King Abdullah University of Science and Technology (KAUST) and supported by KAUST Office of Sponsored Research (OSR) under Award No: CRF-2015-2549-CRG4.

References:

zhu@bnl.gov; jzhu@mail.tsinghua.edu.cn
SC and JL contributed equally to this work

[1] T. W. B. Kibble, *Topological defects and the non-equilibrium dynamics of symmetry breaking phase transitions* (Springer, Dordrecht, 2000).

[2] I. A. Ovid'ko and A. E. Romanov, Commun. Math. Phys. **105**, 443 (1986).

[3] T. W. B. Kibble, J. Phys. A: Math. Gen. **9**, 1387 (1976).

[4] N. D. Mermin, Rev. Mod. Phys. **51**, 591 (1979).

[5] H. R. Trebin, Adv. Phys. **31**, 195 (1982).

[6] A. Vilenkin and E. P. S. Shellard, *Cosmic strings and other topological defects* (Cambridge Univ. Press, Cambridge, 2000).

[7] X. Z. Yu, *et al*., Nature **465**, 901 (2010).

[8] H. Das, A. L. Wysocki, Y. Geng, W. Wu, and C. J. Fennie, Nat. Commun. **5**, 2998 (2014).

[9] D. Meier, *et al.*, Nat. Mater. **11**, 284 (2012).

[10] W. Wu, Y. Horibe, N. Lee, S.-W. Cheong, and J. R. Guest, Phys. Rev. Lett. **108**, 077203 (2012).

[11] O. D. Lavrentovich, Liquid Crystals **24**, 117 (1998).

[12] M. Fiebig, T. Lottermoser, D. Fröhlich, A. V. Goltsev, and R. V. Pisarev, Nature (London) **419**, 818 (2002).

[13] F. -T. Huang, X. Y. Wang, S. M. Griffin, Y. Kumagai, O. Gindele, M. –W. Chu, Y. Horibe, N. A. Spaldin, S. –W. Cheong, Phys. Rev. Lett. **113**, 267602 (2014).

[14] S. Brazovski, N. Kirova, Le Journal de Physique IV, **9**, 10, (1999).

[15] I. E. Dzyaloshinskii, JETP Lett. **25**, 2, (1977).

[16] T. Choi *et al.*, Nat. Mater. **9**, 253-258 (2010).

[17] B. B. Van Aken, T. T. M. Palstra, A. Filippetti, and N. A. Spaldin, Nat. Mater. **3**, 164 (2004).

[18] Y. Kumagai, and N. A. Spaldin, Nat. Commun. **4**, 1540 (2013).

[19] S. M. Griffin *et al.*, Phys. Rev. X **2**, 041022 (2012).

[20] S.-Z. Lin *et al.*, Nat. Phys. **10**, 970 (2014).

[21] M. Lilienblum, *et al.*, Nat. Phys. **11**, 1070 (2015).

[22] J. Li, F.-K Chiang, Z. Chen, C. Ma, M. –W Chu, C. –H Chen, H. F. Tian, H. X. Yang, J. Q. Li, Sci. Rep. **6**, 28047 (2016).

[23] M.-G. Han *et al.*, Adv. Mater. **25**, 2415 (2013).

[24] J. Li *et al.*, Phys. Rev. B **87**, 094106 (2013).

[25] S. C. Chae, Y. Horibe, D. Y. Jeong, S. Rodan, N. Lee, S. –W. Cheong, Proc, Natl. Acad. Sci.

107, 21366, (2010)

[26] F. Xue, X. Y. Wang, I. Socolenco, Y. J. Gu, L. –Q. Chen, S. –W. Cheong, Sci. Rep. **5**, 17057 (2015).

[27] See Supplemental Material [url], which includes Refs. [28-34], for additional details.

[28] Z. C. Wang, M. Saito, K. P. McKenna, Y. Ikuhara, Nat. Comm. **5**, 3239 (2014).

[29] C. W. Zhao, Y. M. Xing, C. E. Zhou, P. C. Bai, Acta Mater. **56**, 2570 (2008).

[30] Y. Y. Zhu, C. Ophusb, J. Cistonb, H. Y. Wanga, Acta Mater. **61**, 5646 (2013).

[31]G. Bárcena-González, M. P. Guerrero-Lebrero, E. Guerrero, D. Fernández-reyes, D. González, A. Mayoral, A. D. Utrilla, J. M. Ulloa, P. L. Galindo, J. Microscopy, **1**, 262 (2015).

[32] M. Arredondo, Q. M. Ramasse, M. Weyland, R. Mahjoub, I. Vrejoiu, D. Hesse, N. D. Browning, M. Alexe, P. Munroe, V. Nagarajan, Adv. Mater. **22**, 2430 (2010).

[33] J. Li, C. Zhao, Y. Xing, S. Su, B. Cheng, Materials, **6**, 6 (2013).

[34] A. M. Sanchez, P. L. Galindo, S. Kret, M. Falke, R. Beanland, P. J. Goodhew, J. Microscopy, **221**, 1 (2006).

[35] M. J. Hÿtch, E. Snoeck, and R. Kilaas, Ultramicroscopy **74**, 3 (1998).

[36] S. Cheng, Y. G. Zhao, X. F. Sun, and J. Zhu, J. Am. Ceram. Soc. **97**, 11 (2014).

[37] C. J. Fennie and K. M. Rabe, Phys. Rev. B **72**, 100103(R) (2005).

[38] S. Artyukhin, K. T. Delaney, N. A. Spaldin, and M. Mostovoy, Nat. Mater. **13**, 42 (2013).

[39] R. Peierls, Proc. Phys. Soc. London **52**, 34 (1940).

[40] F. R. N. Nabarro, Proc. Phys. Soc. London **59**, 256 (1947).

[41] Z. S. Dong and C. W. Zhao, Physica B **405**, 171 (2010).

[42] R. Kutka, H.-R. Trebin, Journal de Physique Letters, **45** (23), 1119 (1984).

[43] R. Kutka, H.-R. Trebin, and M. Kiemes, Journal de Physique, 1989, **50** (8), 861 (1989).

[44] H. R. Trebin, Adv. Phys. **31**, 195 (1982).

[45] V. P. Mineev, *Topologically stable defects and solitons in ordered media*, (Harwood Acad. Publ., 1998)

Figures and Captions:
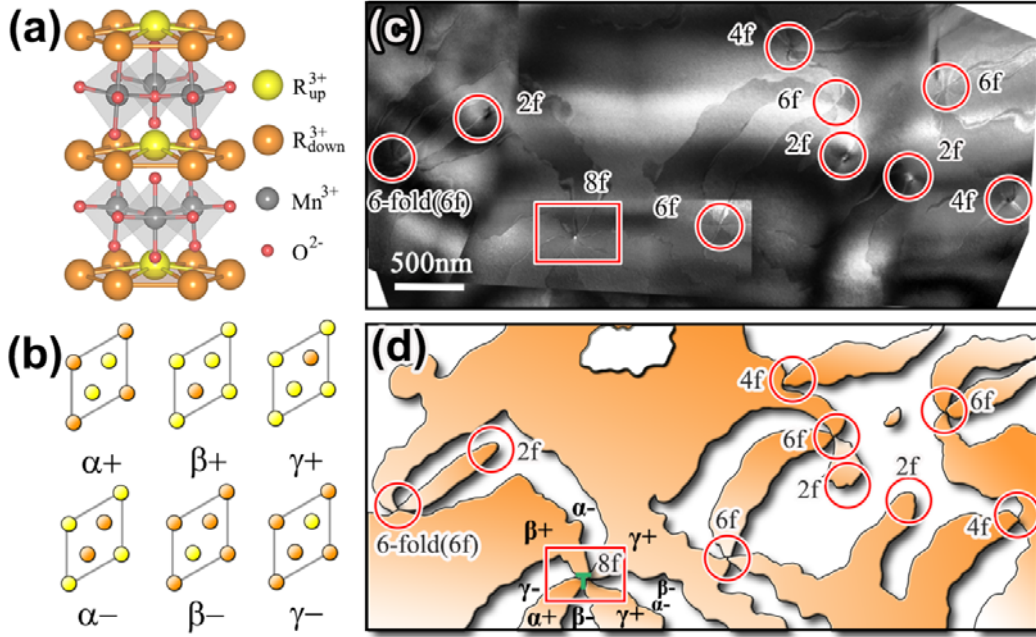
FIG. 1 Non-six-fold vortex domains in hexagonal RMnO$_3$. (a) Atomic unit-cell showing the $P6_3cm$ symmetry with downward polarization. The yellow and orange spheres represent R ions at 2a and 4b Wyckoff positions, respectively. (b) Atomic models for three types of antiphase domains (α, β, γ) and two types of ferroelectric polarizations (+, -). (c) Composite of mesoscale dark-field TEM images with 2-, 4-, 6- and 8-fold vortices, marked by red circles and rectangle in YMnO$_3$. (d) The corresponding schematic diagram from (c).
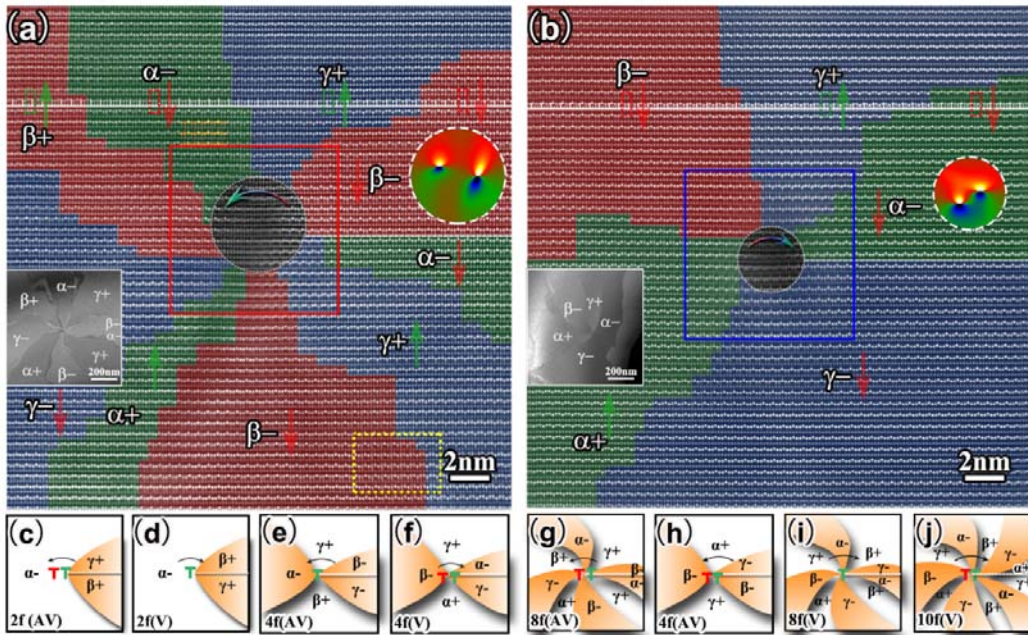

FIG. 2 Atomic images and schematic diagrams of non-six-fold vortices. (a)-(b) High

resolution HAADF-STEM images of eight-fold antivortex (a) and four-fold vortex (b) structures viewed along the [100] axis in $YMnO_3$. The bright and less-bright atoms are Y and Mn ions, respectively. The white horizontal lines with tick marks in (a) and (b) are reference rulers to assist in identifying the translation relationship across the domain walls (small green and red dashed rectangles represent the unit-cell with downward or upward polarization). Low magnification dark-field images and strain maps, where yellow, red, green and blue represent the ε_{xx} values of +8%, +4%, -4% and -8%, respectively, of the core areas are also included. The α, β and γ is colored in green, red and blue, respectively. The red, blue solid squares and yellow dotted rectangle are magnified.[27] (c)-(j) Schematics of eight possible non-six-fold vortices. The first five (c)-(g) are experimentally observed. AV: antivortex, V: vortex. Vortices shown in (a) and (b) can be topologically classified as $(-2) \times (-2)$ and $0 \times (-2)$, and (c)-(j) can be classified as $(-1) \times (-2)$, $0 \times (-1)$, $(-1) \times (-1)$, $0 \times (-2)$, $(-2) \times (-2)$, $(-1) \times (-2)$, $1 \times (-1)$ and $1 \times (-2)$, respectively. The horizontal lines in (a)-(j) are the dividing line for order parameter θ.
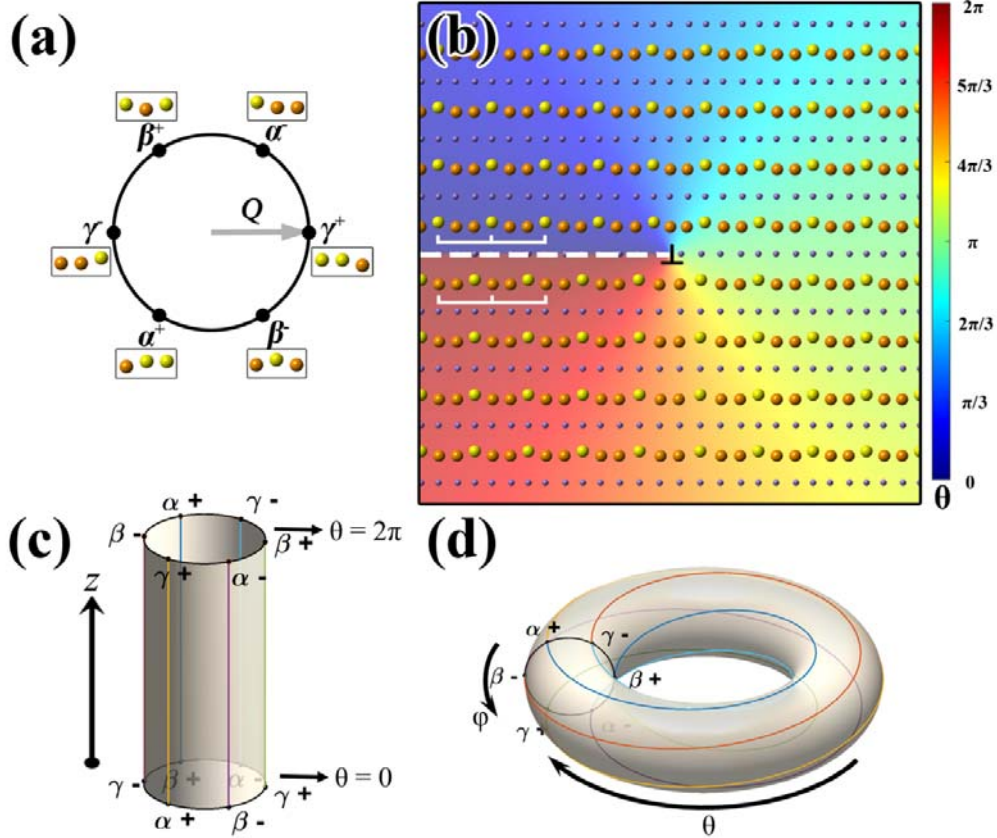
FIG. 3 (a) The order parameter (OP) space of a dislocation-free system. The six black points represent six degenerate states with Z_6 symmetry at low temperatures. The corresponding corrugated configurations of R atoms are also shown. Degeneracy space expands to the circle with continuous $U(1)$ symmetry as temperature rises. The radius of this circle is proportional

to Q. (b) A schematic shows the atomic structure around an edge dislocation with $b = 1$ in a mono-domain. The field of OP θ is represented by the color legend. The dividing line (doted white line) indicates the position where θ discontinues. (c) The OP space of the RMnO$_3$ system in which dislocations (vertical lines) exist. The value of θ varies from 0 to 2π along the z axis. (d) A torus-like OP space obtained by transforming the cylinder shown in (c): the two ends of this cylinder can be equivalent by twisting the cylinder (the α$^+$ point on the upper end aligns with the lower one along the z axis). With fixed θ, the variation of φ from 0 to 2π corresponds to a loop passing once through the smaller hole in the torus (the black circle). Similarly, as θ varies from 0 to 2π with φ = 0, its corresponding trajectory is the yellow line on the torus.
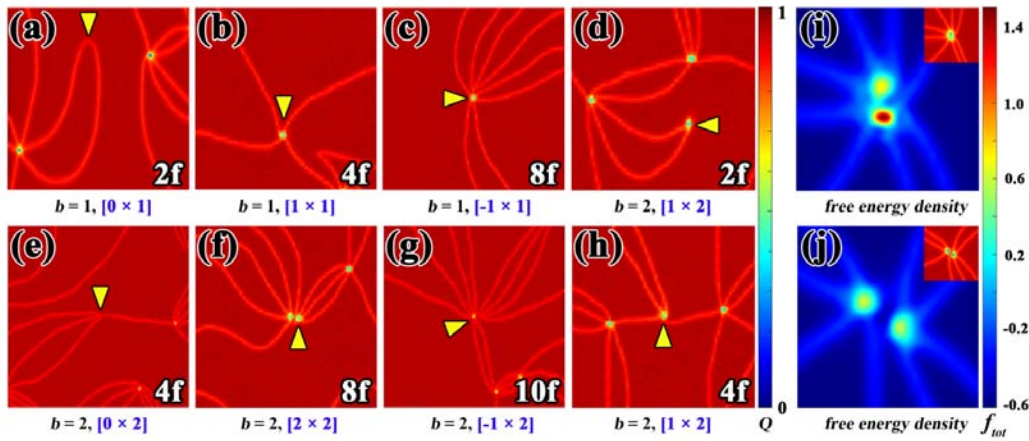
FIG. 4 Numerical simulations based on the Landau free energy model. (a)-(h) Coexistence of six-fold vortices and eight other types of dislocation-induced vortices, showing the tilting amplitude Q of the OP field around the vortex cores. The yellow arrows indicate the position of dislocations. Corresponding Burgers vectors b and fundamental homotopy group elements $[m \times n]$ are given at the bottom of each figure. Since the value of Q is slightly smaller at domain walls than within domains, the bright-red lines indicate the position of domain walls. Because of the high gradient free energy density in some types of vortex cores (b, c, d, f, g, and h), Q decreases dramatically within these cores, which appear as yellow/green spots in these figures. By contrast, Q does not obviously decrease within vortex cores where the density is relative low (a, e). Two spots are observed in (f) because the core is not stable and tends to split into two sub-cores. The color legend of Q is shown on the right with units of Å. (i) and (j) show the free-energy-density distributions around two 2 × 2 type eight-fold vortex cores obtained at two different dislocation formation temperatures T_d. The fission of vortex core contributes to a reduction of the local free energy. Corresponding distributions of Q are given at the top right. The color legend of free energy density is shown on the right with unit of eV.